IUST
Iran University of Science and Technology

Iranian Journal of Electrical and Electronic Engineering

Journal Homepage: ijeee.iust.ac.ir

Research Paper

An Improved Magnetic Equivalent Circuit Model for Electromagnetic Modeling of Electric Machines

F. Rezaee-Alam*(C.A.), B. Rezaeealam*, and S. M. M. Moosavi**

Abstract: Poor modeling of air-gap is the main defect of conventional magnetic equivalent circuit (CMEC) model for performance analysis of electric machines. This paper presents an improved magnetic equivalent circuit (IMEC) which considers all components of air-gap permeance such as the mutual permeances between stator and rotor teeth, and the leakage permeances between adjacent stator teeth and adjacent rotor teeth in the air-gap. Since the conformal mapping (CM) method can accurately take into account the air-gap region, IMEC gets help from the CM method for calculating the air-gap permeance components. Therefore, the obtained model is a hybrid analytical model, which can accurately take into account the magnetic saturation in iron parts by using the CMEC, and the real paths of fringing flux, leakage flux, and the main flux in the air-gap by using the CM method. For a typical wound rotor induction motor, the accuracy of the results obtained by IMEC is verified by comparing them with the corresponding results determined through CMEC, improved conformal mapping (ICM), finite element method (FEM), and the experiment results.

Keywords: Improved Magnetic Equivalent Circuit (IMEC), Conformal Mapping (CM), Conventional Magnetic Equivalent Circuit (CMEC), Magnetic Saturation, Permeance.

1 Introduction

ACCURATE and fast modeling techniques are necessary for design, optimization, and control of electric machines. The accurate modeling of electric machines is possible by using the finite element method (FEM) [1]. However, FEM is a time-consuming method, and it is better to be only used in the final stage for verifying the results. Moreover, the user cannot find an in-depth knowledge of the performance of electric machines while using the FEM. To this end, different techniques have been so far introduced such as winding function theory (WFT) [2, 3], conventional magnetic equivalent circuit (CMEC) model [4-6], conformal mapping (CM) method [7-9], field reconstruction method (FRM) [10, 11], and sub-domain (SD) model [12, 13].

However, the above-mentioned techniques have some defects. The conventional WFT alone cannot take into account the slotting effect and the magnetic saturation [2, 3]. The FRM is based on superposition principle. Therefore, FRM cannot consider the nonlinearity effects such as the magnetic saturation [10]. In the SD model, the geometry of electric machine is divided into four domains including slot, slot opening, permanent magnet (PM), and air-gap. The Laplace/Poisson equations are then solved in each domain separately, and the final result is then obtained by applying the boundary conditions on the interface between the domains [13]. However, the SD model is suitable only for geometries with radial and tangential boundaries. The CM method is based on complex analysis [7] and its main advantage is its capability in the precise modeling of slotted air-gap. However, the CM method cannot take into account the magnetic saturation. The CMEC model can accurately model the saturation effect in iron parts whereas its main defect is

Iranian Journal of Electrical and Electronic Engineering, 2021.
Paper first received 22 August 2020, revised 09 December 2020, and accepted 09 December 2020.
* The authors are with the Department of Electrical Engineering, Lorestan University, Khorramabad, Lorestan 68151-44316, Iran.
E-mails: rezaee.fa@lu.ac.ir and rezaee.bh@lu.ac.ir.
** The author is with the Department of Electrical Engineering, Hamedan University of Technology, Hamedan 65155, Iran.
E-mail: moosavi@hut.ac.ir.
Corresponding Author: F. Rezaee-Alam.
https://doi.org/10.22068/IJEEE.17.3.1965

poor modeling of slotted air-gap [4-6].

According to the above discussions, the analytical and semi-analytical models have some defects and advantages, simultaneously. Therefore, these models can be combined in order to remove the existing defects [14, 20]. The hybrid analytical model (HAM) presented in [14] employs the CMEC model for converting the 3-D FEM model into the equivalent 2-D FEM model. The CMEC model can consider the iron parts whereas the field solution in the air-gap is simultaneously obtained through solving Maxwell's equations [15]. In [16], CM was used to consider the slotting effect in the slotless CMEC model of multi-layered interior PM motor. The CM was also used to calculate the reluctance of flux barriers of synchronous reluctance machines for using in the CMEC model [17, 18]. The technique based on the CM was presented in [19] which considers the magnetic saturation in iron parts by using equivalent line currents obtained through the CMEC. The HAM presented in [20] is also based on the FRM assisted by the CM method for considering the slot impact. Due to the complex geometry of multi-layer interior PM motor, the rotor magnetic field has been obtained in [21] through the CMEC model, and the magnetic field in the stator slots, slot openings, and air-gap have been obtained from the SD model.

This paper presents an improved MEC (IMEC) model for a typical wound rotor induction motor (WRIM), which considers the air-gap region and iron parts by using the CM and CMEC, respectively. IMEC is also applicable to all electric machines. The outline of this paper is as follows: The CMEC and CM methods are respectively introduced in Sections 2 and 3. The components of the air-gap permeances and their calculation methods are presented in Section 4. An improved CM method is introduced in Section 5. The results obtained through the CMEC, CM/ICM, IMEC, FEM, and experimental results are compared in Section 6. Section 7 concludes the paper.

2 Conventional Magnetic Equivalent Circuit (CMEC)

Table 1 shows the rated parameters of the typical WRIM studied in this paper. Fig. 1 shows a part of the CMEC model for the WRIM. The algebraic equations of the CMEC model of the WRIM are obtained by using the nodal analysis as follows:

$$A_{sy}U_{sy} = -\Phi_{st} \tag{1}$$

$$A_{ss}U_{st} + A_{sr}U_{rt} = \Phi_{st} \tag{2}$$

$$A_{rs}U_{st} + A_{rr}U_{rt} = \Phi_{rt} \tag{3}$$

$$A_{rs} = \left(A_{sr}\right)^T \tag{4}$$

$$A_{ry}U_{sy} = -\Phi_{rt} \tag{5}$$

$$U_{st} - U_{sy} - F_{st} = -R_{st}\Phi_{st} \tag{6}$$

$$U_{rt} - U_{ry} - F_{rt} = -R_{rt}\Phi_{rt} \tag{7}$$

where A_{sy}, A_{ss}, A_{sr}, A_{rr}, and A_{ry} are respectively the permeance matrix of the stator yoke, the permeance matrix in the stator nodes on the surface of air-gap, the permeance matrix between the stator and rotor teeth, the permeance matrix in rotor nodes on the surface of the air-gap, and the permeance matrix of the rotor yoke. U_{sy}, U_{st}, U_{rt}, and U_{ry} are the magnetomotive force (MMF) matrix in the nodes of stator yoke, stator and rotor teeth on the surface of the air-gap, and the rotor yoke, respectively. Φ_{st}, R_{st}, Φ_{rt}, and R_{rt} are the matrix of magnetic flux and reluctance of stator and rotor teeth, respectively.

Table 1 Main parameters for analyzed WRIM.

Parameter	Value and unit
Number of pole pairs, p	2
Number of stator slots, N_s	36
Number of rotor slots, N_r	24
Rated power, P	4 kW
Rated stator voltage, V	400 V
Rated speed	1420 rpm
Rated frequency, f	50 Hz
Stator outer diameter	200 mm
Stator inner diameter	136 mm
Active length, L	114 mm
Air gap length, g	0.5 mm
Stator turns per coil, N_{cs}	30
Rotor turns per coil, N_{cr}	27
Stator tooth width	6 mm
Rotor tooth width	9.3 mm

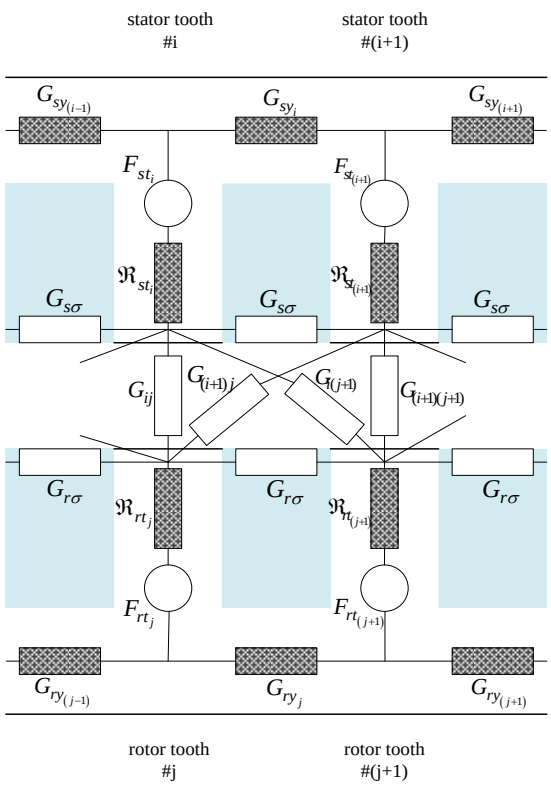

Fig. 1 CMEC model of the analyzed WRIM [6].

The MMF sources of stator and rotor are calculated as follows:

$$F_{st} = W_s I_s \tag{8}$$

$$F_{rt} = W_r I_r \tag{9}$$

where W_s, I_s, W_r, and I_r are the MMF transform matrix and the phase current vector of stator and rotor, respectively.

The flux-linkage equations of the stator and rotor are as follows:

$$\frac{d\lambda_s}{dt} = V_s - R_s I_s \tag{10}$$

$$\frac{d\lambda_r}{dt} = -R_r I_r \tag{11}$$

where λ_s and λ_r are the flux-linkage of the stator and rotor phases, R_s and R_r are the resistance matrix of the stator and rotor phases, and V_s is the vector of input voltage of stator winding. The system of equations (1)-(11) is nonlinear due to the magnetic saturation in iron parts. At this end, the solution of this system of equations includes an internal loop and an external loop. The external loop includes the solution of (10) and (11) for each simulation time. In fact, the zero-initial value is considered for λ_s, λ_r, and consequently $\emptyset_{st}$, $\emptyset_{rt}$. Therefore, their values for the next step are calculated as follows:

$$\lambda_s(k+1) = \lambda_s(k) + \Delta t\left(V_s(k) - R_s I_s(k)\right) \tag{12}$$

$$\lambda_r(k+1) = \lambda_r(k) - \Delta t R_s I_s(k) \tag{13}$$

$$\varnothing_{st}(k+1) = \left(W_s^T\right)^{-1}\lambda_s(k+1) \tag{14}$$

$$\varnothing_{rt}(k+1) = \left(W_r^T\right)^{-1}\lambda_r(k+1) \tag{15}$$

The magnetic operating point is unknown for each time-step of the simulation; therefore, an internal loop should be used to iteratively solve the nonlinear system of equations (1)-(9). The Newton-Raphson method can be applied here. After converging the solution in each time-step, the electromagnetic torque and rotor speed of WRIM can be calculated as follows:

$$T_e(\theta_r) = \sum_{i=1}^{N_s}\sum_{j=1}^{N_r}\left(U_{2,i} - U_{3,j}\right)^2 \frac{dA_{23}(i,j)}{d\theta_r} \tag{16}$$

$$T_e(\theta_r) - T_l = J\frac{d\omega_r}{dt} + D\omega_r \tag{17}$$

$$\omega_r = \frac{d\theta_r}{dt} \tag{18}$$

where t is the simulation time in second, θ_r is the rotor position in radian, ω_r is the rotor speed in radian per second, J is the inertia of rotor in kg.m^2, D is the friction coefficient in Nms/rad, and T_e is the electromagnetic torque in Nm.

3 Conformal Mapping (CM) Method

The CM method is based on complex analysis [9]. In fact, the CM method is an analytical or semi-analytical technique that converts the slotted geometry of electric machine into the slotless geometry in order to calculate the relative complex permeance of the slotted air-gap (Λ_s).

The general algorithm of the CM method is calculation of the slotless air-gap magnetic field, and then using the relative complex permeance for evaluation of the slotted air-gap magnetic field as follows:

$$B_s = B_\psi \times \left(\Lambda_s\right)^* \tag{19}$$

$$\Lambda_s = \Lambda_r + j\Lambda_t \tag{20}$$

where Λ_r and Λ_t are respectively the radial and tangential components of the relative complex permeance of the slotted air-gap, B_ψ and B_s are the slotless and slotted air-gap flux density.

3.1 Calculation of Slotless Air-Gap Magnetic Field

Hague's solution is a well-known technique to calculate the scalar magnetic potential in the slotless air-gap. In order to apply this technique, the stator and rotor windings are modeled with equivalent line currents. According to this technique, the scalar magnetic potential due to one line current in an annular domain (Fig. 2) is calculated as follows [7, 8]:

$$\Omega = \begin{cases} \frac{I}{2} + \sum_{n=1}^{\infty}\left(\left(A_n - \frac{I}{2n\pi c^n}\right)r^n + B_n r^{-n}\right), & r < c \\ \frac{I(\Delta\theta+\pi)}{4\pi} + \sum_{n=1}^{\infty}\left(A_n r^n + B_n r^{-n}\right)\sin\left(n(\Delta\theta)\right), & r = c \\ \frac{I\Delta\theta}{2\pi} + \sum_{n=1}^{\infty}\left(A_n r^n + \left(\frac{Ic^n}{2n\pi} + B_n\right)r^{-n}\right)\sin\left(n(\Delta\theta)\right), & r > c \end{cases}$$

$$\begin{cases} A_n = \dfrac{-I(\mu_1-\mu_2)\left\{b^{2n}(\mu_3-\mu_2) + c^{2n}(\mu_3+\mu_2)\right\}}{c^n 2n\pi\left(b^{2n}(\mu_1-\mu_2)(\mu_2-\mu_3) + a^{2n}(\mu_1+\mu_2)(\mu_2+\mu_3)\right)} \\ B_n = \dfrac{b^{2n} I(\mu_3-\mu_2)\left\{c^{2n}(\mu_1-\mu_2) + a^{2n}(\mu_1+\mu_2)\right\}}{c^n 2n\pi\left(b^{2n}(\mu_1-\mu_2)(\mu_2-\mu_3) + a^{2n}(\mu_1+\mu_2)(\mu_2+\mu_3)\right)} \\ \Delta\theta = \theta - \theta_I \end{cases} \tag{21}$$

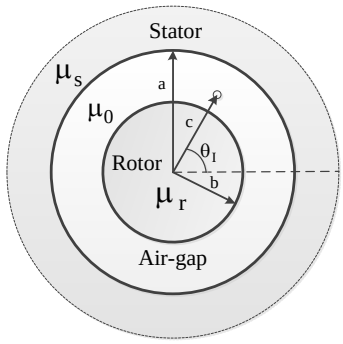

Fig. 2 Annular domain for field calculation.

where $ce^{j\theta_l}$ is the coordinate of typical line current with the magnitude of I, and $re^{j\theta}$ is the coordinate of the desired point in annular air-gap. Other parameters are illustrated in Fig. 2.

Hague's solution necessitates the mapping of the physical slotless model of WRIM to the canonical slotless model, so that the values of $b \le r \le a$ have to be very close to 1. The air-gap flux density is then calculated as follows [7, 8]:

$$B_{slotless} = -\mu_0 \nabla \Omega = -\mu_0 \left[\frac{\partial \Omega}{\partial r} \vec{a_r} + \frac{1}{r} \frac{\partial \Omega}{\partial \theta} \vec{a_\theta} \right] \tag{22}$$

Similarly, the air-gap flux density is calculated for all line currents due to the stator and rotor windings.

3.2 Calculation of Relative Complex Permeance

The relative complex permeance was initially introduced in [22, 23] for surface-mounted PM motors. However, the calculation of relative complex permeance is more complicated for WRIMs due to both slotted stator and rotor cores. To this end, the technique presented in this paper can only include a fraction of motor geometry while considering the finite depth of slots and the interaction effect between adjacent slots. Therefore, this technique can also be efficiently used to calculate the relative complex permeance for high power electric machines that have a lot of slots. For simplicity, it is necessary to separately calculate the relative complex permeance due to the slotting effect of the stator and rotor. The relative complex permeance is generally defined as follows:

$$\Lambda_s = \frac{\Lambda_{st}}{\Lambda_{sl}} = \Lambda_r + j\Lambda_t \tag{23}$$

where Λ_{st} and Λ_{sl} are the complex permeance of the slotless and slotted air-gap, respectively.

To calculate the relative complex permeance of the slotted air-gap, the following steps should be followed, which are shown in Fig. 3.

1) The zoomed view of motor geometry including only the stator slots is considered in S-plane.
2) The motor geometry in S-plane is mapped into Z-plane using CM_1. Fig. 4(a) shows a quarter of the air-gap polygon in the Z-plane.
3) CM_2 is used to transform the air-gap polygon in Z-plane into the canonical rectangle in W-plane. CM_2 is the Schwartz-Christoffel (SC) mapping, which is numerically solved using the SC Toolbox [24] while considering all corners in air-gap polygon in Z-plane. Fig. 4(b) shows a quarter of the air-gap polygon in the W-plane.
4) CM_3 is used to transform the canonical rectangle in W-plane into an annulus in Ψ-plane. In relation of CM_3, coefficient C in ($0 < C < 1$) shows the fraction C of motor geometry has only been considered
5) Considering only the stator slotting, the air-gap complex permeance is calculated as follows:

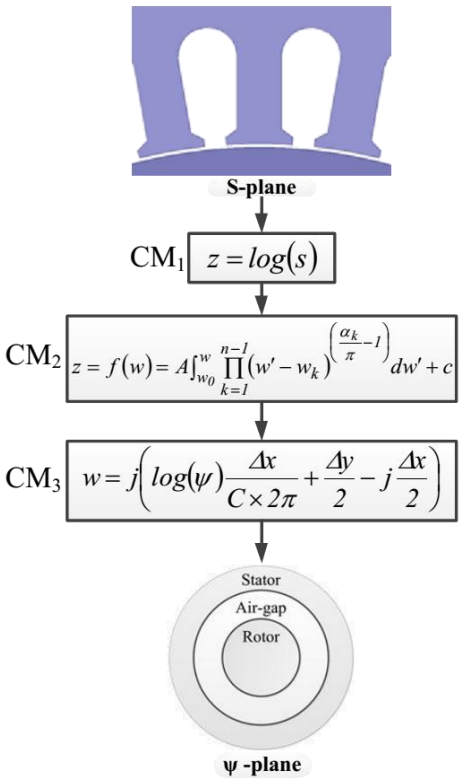

Fig. 3 CMs used for geometrical transformation.

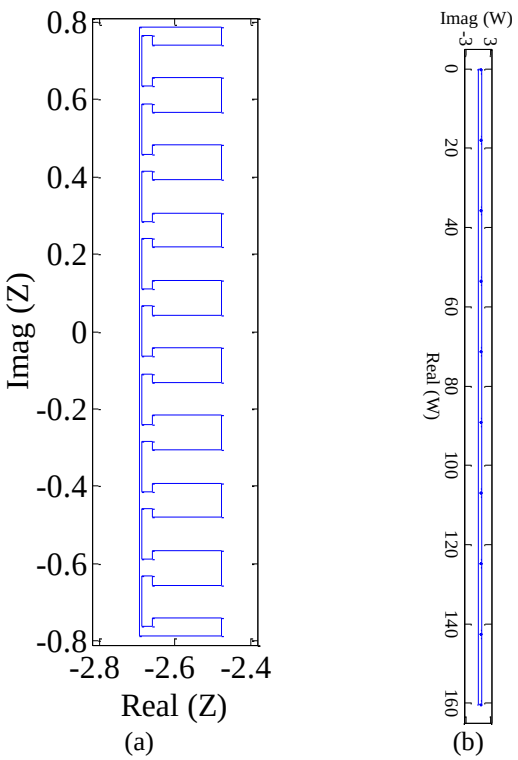

Fig. 4 CMs used for geometrical transformation; a) Z-plane and b) W-plane.

$$\Lambda_{st} = \left(\frac{\partial \psi}{\partial w} . \frac{\partial w}{\partial z} . \frac{\partial z}{\partial s} \right)_{slotted} \tag{24}$$

6) Considering the slotless geometry of motor in S-plane (Fig. 3), the complex permeance for the slotless air-gap (Λ_{sl}) is also calculated as follows:

$$\Lambda_{sl} = \left(\frac{\partial \psi}{\partial w} . \frac{\partial w}{\partial z} . \frac{\partial z}{\partial s} \right)_{slotless} \tag{25}$$

where $\frac{\partial z}{\partial s} = \frac{1}{s}$, $\frac{\partial w}{\partial z}$ is calculated using the command "*evaldiff*" in SC Toolbox as follows:

$\frac{\partial w}{\partial z} = \frac{1}{evaldiff\ (f, W)}$, f is the SC mapping $z = f(w)$

$$\frac{\partial \psi}{\partial w} = -j \left(\frac{2\pi}{\Delta x} \right) e^{-j\left(\frac{2\pi}{\Delta x}\right)\left(W - \frac{\Delta x}{2} - j\frac{\Delta y}{2}\right)}$$

Considering a contour in the middle of air-gap in S-plane as $S_g = R_g\, e^{j\alpha}$, Λ_{st} and Λ_{sl} are calculated on this contour as follows:

$$\Lambda_{st} = \left(\frac{1}{S_g} \right) \times \left(\frac{1}{evaldiff\ (f_{st}, W_{g,st})} \right) \times \left(-j \left(\frac{2\pi}{\Delta x_{st}} \right) e^{-j\left(\frac{2\pi}{\Delta x_{st}}\right)\left(W_{g,st} - \frac{\Delta x_{st}}{2} - j\frac{\Delta y_{st}}{2}\right)} \right) \tag{26}$$

$$\Lambda_{sl} = \left(\frac{1}{S_g} \right) \times \left(\frac{1}{evaldiff\ (f_{sl}, W_{g,sl})} \right) \times \left(-j \left(\frac{2\pi}{\Delta x_{sl}} \right) e^{-j\left(\frac{2\pi}{\Delta x_{sl}}\right)\left(W_{g,sl} - \frac{\Delta x_{sl}}{2} - j\frac{\Delta y_{sl}}{2}\right)} \right) \tag{27}$$

where Δx_{st} and Δy_{st} are respectively the length and the width of canonical rectangle of slotted air-gap in W-plane. f_{st} is the SC mapping which is used to transform the polygon of slotted air-gap in Z-plane into the canonical rectangle, and $W_{g,st}$ is calculated as

$$\begin{cases} W_{g,st} = evalinv\ (f_{st}, Z_g) \\ Z_g = \log(S_g) \end{cases} \tag{28}$$

"*evalinv*" is also one of the commands in SC Toolbox.

7) The relative complex permeance of the slotted air-gap due to the stator slotting is then calculated by using (23).

Similarly, the relative complex permeance due to the rotor slotting can also be calculated. Fig. 5 shows the radial and tangential components of Λ_s for the stator and rotor slotting in one pole pitch. Finally, the relative complex permeance of the slotted air-gap is calculated as follows:

$$\begin{cases} \Lambda_s(\varphi_s, \theta_r) = \Lambda_{stator}(\varphi_s) \times \Lambda_{rotor}(\varphi_s, \theta_r) \\ \qquad = \Lambda_r(\varphi_s, \theta_r) + j\,\Lambda_t(\varphi_s, \theta_r) \\ \Lambda_r = \Lambda_{r_stator} \times \Lambda_{r_rotor} - \Lambda_{t_stator} \times \Lambda_{t_rotor} \\ \Lambda_t = \Lambda_{r_stator} \times \Lambda_{t_rotor} + \Lambda_{t_stator} \times \Lambda_{r_rotor} \end{cases} \tag{29}$$

where φ_s is the circumferential coordinate in the air-gap.

3.3 Algorithm of CM Method

The general algorithm of the CM method is as follows:

a) The rated three-phase voltages are applied to the stator windings.
b) Zero initial currents are considered for stator and rotor phase windings.
c) The stator and rotor windings are modeled by

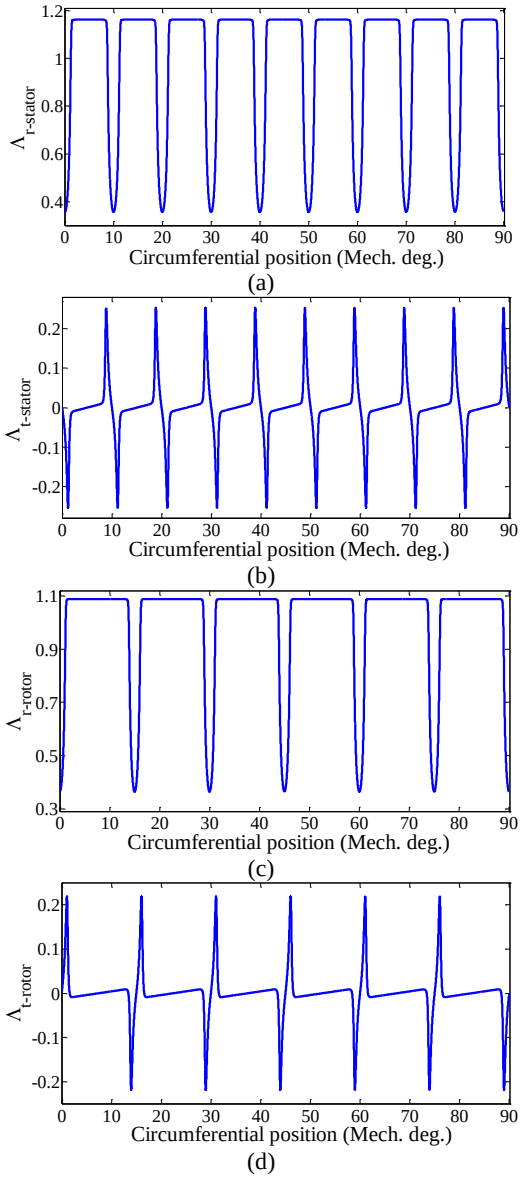

Fig. 5 Components of relative complex air-gap permeance.

equivalent line currents as shown in Fig. 6. All conductors in each slot layer are replaced with an equivalent line current as

$$I_e = n_c I_c \tag{30}$$

where n_c is the number of conductors in the respective slot layer, I_c is the current of each conductor, and I_e is the magnitude of equivalent line current which is calculated in each time-step of simulation.

d) Slotless model of WRIM is prepared in S-plane while considering the equivalent line currents in respective positions in inner surface of stator and outer surface of rotor core.

e) By using the CMs introduced in Fig. 3, the physical slotless model of WRIM in S-plane (including equivalent line currents) is mapped into the canonical slotless model in ψ-plane. The inner and outer radii of slotless model in ψ-plane are very close to "1", and this is the necessary condition for using Hague's solution. Slotless air-gap flux density in ψ-plane (B_ψ) is then calculated using Hague's solution.

f) Slotless complex air-gap permeance (Λ_{sl}) is only once calculated by using (25) and (28).

g) Slotless air-gap flux density in S-plane (B_{s_sl}) is then calculated as

$$B_{s_sl} = B_\psi \times \left(\Lambda_{sl}\right)^* \tag{31}$$

h) Slotted complex air-gap permeance (Λ_{st}) is only once calculated by using (24).

i) The components of relative complex permeance of slotted air-gap (Λ_r, Λ_t) is only once calculated by using (30).

j) Slotted air-gap flux density in S-plane (B_{s_st}) is then calculated as

$$B_{s_st} = B_{s_sl} \times \left(\Lambda_s\right)^* \tag{32}$$

k) The self and mutual inductances versus the rotor position are calculated using the conventional method.

l) Phase currents of stator and rotor are then calculated for the next time-step of simulation through simultaneous solving the mechanical and electrical equations.

Fig. 7 shows the flowchart of simulation by the CM method.

4 Improved Magnetic Equivalent Circuit (IMEC) Model

In the CMEC model, the air-gap permeances are calculated using Ostovic's method, which merely accounts for the smoothing effect of fringing flux tubes [25]. In [26-28], the fringing flux tubes are included more explicitly than [25].

The inclusion of fringing flux tubes would yield a larger value for air-gap permeance than that given by Ostovic's method. In [29], a rough formula was also presented for calculating the leakage air-gap permeance between adjacent stator teeth, which cannot consider the impact of slot opening, and so it underestimates the respective leakage permeance. All techniques presented in [25-29] are more or less empirical techniques and take into account the fringing flux, leakage flux, and the flux entered to the slot from air-gap, approximately. Therefore, the CMEC model and other empirical techniques cannot accurately consider the air-gap region. At this end, the IMEC gets help from the CM method to calculate the air-gap permeances, which can accurately consider the air-gap flux tubes. IMEC

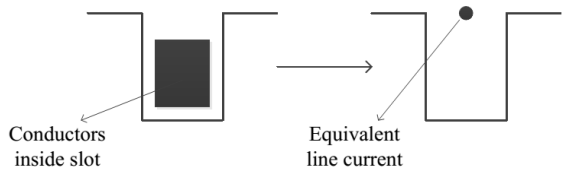

Fig. 6 Equivalent line current of slot conductors.

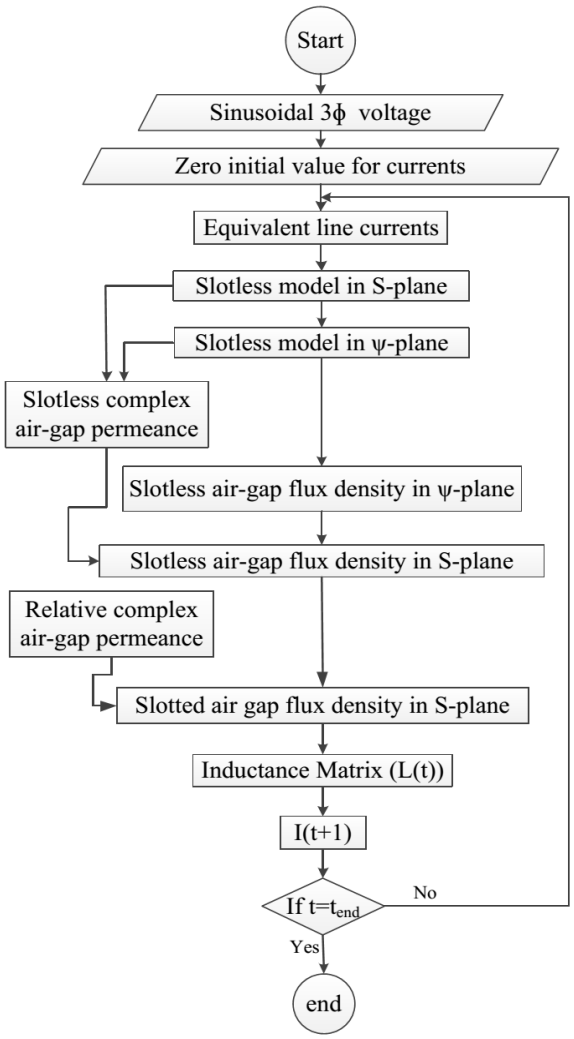

Fig. 7 Simulation flow-chart by CM.

considers the magnetic saturation in iron parts similar to the CMEC.

The air-gap permeances are divided into two general groups as follows:

- The mutual air-gap permeances between the stator and rotor teeth.
- The leakage air-gap permeances between adjacent stator/rotor teeth.

4.1 Calculation of Mutual Air-Gap Permeances

Fig. 8 shows the air-gap flux-tubes crossing stator to the rotor and vice versa. Since the MMF drop in the iron parts between adjacent flux tubes is negligible, the air-gap flux tubes between the opposite stator and rotor teeth are in parallel.

Therefore, the total air-gap permeance between *i*-th tooth of the stator and *j*-th tooth of the rotor is calculated as follows:

$$G_{i,j}(\theta_r) = \int dG = G_b \int_0^{2\pi} n_{m,i}(\varphi_s) n_{m,j}(\varphi_s,\theta_r) \Lambda_{r_stator}(\varphi_s) \Lambda_{r_rotor}(\varphi_s,\theta_r) d\varphi_s \quad (33)$$

where dG is the permeance of a typical flux tube with angular width of $d\varphi_s$, $n_{m,i}(\varphi_s)$ and $n_{m,j}(\varphi_s, \theta_r)$ are respectively the virtual turn functions of *i*-th tooth of the stator and *j*-th tooth of the rotor as defined in (35).

$$n_{m,i}(\varphi_s) = \begin{cases} 1 & \gamma_s \times (i-1) \le \varphi_s \le \gamma_s \times i \\ 0 & \text{otherwise} \end{cases} \quad (34)$$

$$n_{m,j}(\varphi_s,\theta_r) = \begin{cases} 1 & (\gamma_r \times (j-1) + \theta_r) \le \varphi_s \le (\gamma_r \times j + \theta_r) \\ 0 & \text{otherwise} \end{cases} \quad (35)$$

where γ_s and γ_r are the slot pitch of the stator and rotor in radian, respectively. G_b is the slotless permeance between two opposite stator and rotor teeth as follows:

$$G_b = \frac{\mu_0 \times \min(y_s, y_r) \times L}{g} \quad (36)$$

where y_s and y_r are respectively the slot pitch of the stator and rotor in meter.

Fig. 9 compares the mutual air-gap permeance between two opposite stator and rotor teeth in rotor position obtained through the IMEC, CMEC (Ostovic's method) [25], Bash's method [26], and Deihimi's method [27, 28]. As shown, the IMEC shows the stronger magnetic coupling between the stator and rotor teeth. Fig. 9 also shows the angular range of G_{max} obtained through the IMEC is smaller than or equal to it obtained from other techniques. Consequently, CMEC cannot accurately model the fringing flux tubes in air-gap because Ostovic's method approximately considers the effect of flux fringing on the air-gap permeances.

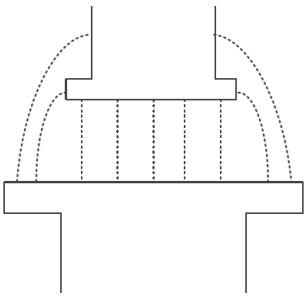

Fig. 8 Magnetic coupling between two opposite teeth.

4.2 Calculation of Leakage Air-Gap Permeances

Fig. 10 shows the leakage flux-tubes between two adjacent stator teeth and two adjacent rotor teeth in the air-gap.

The leakage flux-tubes between adjacent teeth can also be considered in parallel. Therefore, the leakage permeance between adjacent stator teeth and adjacent rotor teeth is calculated as follows:

$$G_{l,(i,i+1)}(\theta_r) = \int dG = G_{b_ts} \int_0^{2\pi} \frac{n_{l,i}(\varphi_s) \Lambda_{t_stator}(\varphi_s)}{\Lambda_{r_rotor}(\varphi_s,\theta_r)} d\varphi_s \quad (37)$$

$$G_{l,(j,j+1)}(\theta_r) = \int dG = G_{b_tr} \int_0^{2\pi} \frac{n_{l,j}(\varphi_s,\theta_r) \Lambda_{t_rotor}(\varphi_s,\theta_r)}{\Lambda_{r_stator}(\varphi_s)} d\varphi_s \quad (38)$$

where $G_{l,(i,i+1)}(\theta_r)$ and $G_{l,(j,j+1)}(\theta_r)$ are respectively the leakage permeances between teeth (i^{th},$(i+1)^{th}$) of the stator and teeth (j^{th},$(j+1)^{th}$) of the rotor. G_{b_ts} and G_{b_tr} are the base values of the air-gap permeance in the tangential direction as follows:

$$G_{b_ts} = \frac{\mu_0 \times g \times L}{y_s} \quad (39)$$

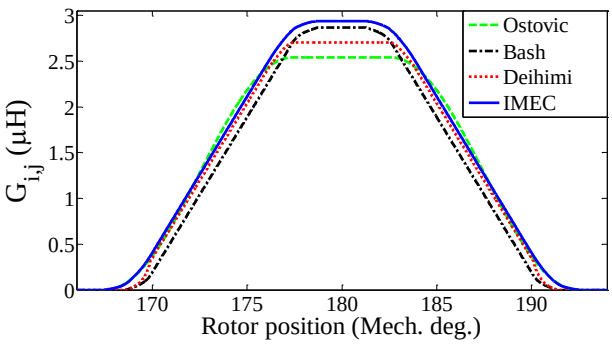

Fig. 9 Mutual permeance between stator and rotor teeth.

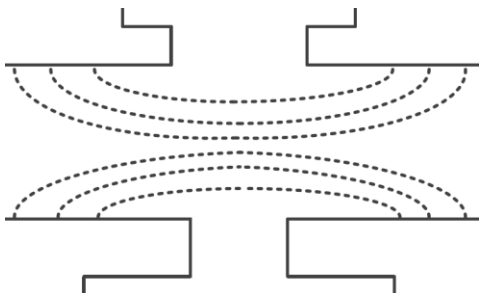

Fig. 10 Magnetic leakage between adjacent teeth.

$$G_{b_tr} = \frac{\mu_0 \times g \times L}{y_r} \tag{40}$$

$n_{l,i}(\varphi_s)$ and $n_{l,j}(\varphi_s, \theta_r)$ are also the virtual turn function of i-th slot-opening of the stator and j-th slot-opening of the rotor as follows ($\varphi_s = 0$ is considered in the center of slot):

$$n_{l,i}(\varphi_s) = \begin{cases} 1 & \gamma_s \times (i-1) + 0.5\gamma_s \le \varphi_s \le \gamma_s \times i + 0.5\gamma_s \\ 0 & \text{otherwise} \end{cases}$$

$$n_{l,j}(\varphi_s, \theta_r) = \begin{cases} 1 & (\gamma_r \times (j-1) + 0.5\gamma_r + \theta_r) \le \varphi_s \\ & \le (\gamma_r \times j + 0.5\gamma_r + \theta_r) \\ 0 & \text{otherwise} \end{cases} \tag{41}$$

Figs. 11(a) and 11(b) show the air-gap leakage permeance between two adjacent teeth of stator and rotor in terms of the rotor position. As shown, the air-gap leakage permeances vary with the rotation of rotor due to the stator or rotor slotting. The air-gap leakage permeances are usually neglected in the CMEC model. As shown in Fig. 1, the CMEC only considers the slot leakages permeances.

5 Improved Conformal Mapping (ICM) Method

The air-gap region can be accurately modeled by CM. However, CM has a main defect in modeling of magnetic saturation. In [30], an ICM was presented for considering the magnetics saturation in stator teeth through increasing the air-gap length in front of teeth. However, the using of this technique necessitates the calculation of relative complex permeance in every rotor position, which is time-consuming. For this reason, another ICM was presented in [31], which considers the MMF drop in iron parts due to magnetic saturation by equivalent virtual currents obtained through the CMEC model.

Figs. 12(a) and 12(b) illustrate the part of the CMEC model of stator and rotor cores, separately. $\Phi_{ts,(i)}$, $\Phi_{os,(i)}$, and $\Phi_{ts,(i+1)}$ show the input flux into the teeth $(i)^{th}$, $(i+1)^{th}$, and opening $(i)^{th}$ of stator. $\Phi_{tr,(i)}$, $\Phi_{or,(i)}$, and $\Phi_{tr,(i+1)}$ also show the input flux into the teeth $(i)^{th}$, $(i+1)^{th}$, and opening $(i)^{th}$ of the rotor, which are calculated by CM method as:

$$\Phi_{ts}(i) = R_s^- .L. \int_{\alpha_{is} - \frac{\gamma_{ts}}{2}}^{\alpha_{is} + \frac{\gamma_{ts}}{2}} B_r(\varphi, \theta_r) d\varphi \tag{42}$$

$$\Phi_{os}(i) = R_s^- .L. \int_{\beta_{is} - \frac{\gamma_{os}}{2}}^{\beta_{is} + \frac{\gamma_{os}}{2}} B_r(\varphi, \theta_r) d\varphi \tag{43}$$

$$\Phi_{tr}(i) = R_r^+ .L. \int_{\alpha_{ir} - \frac{\gamma_{tr}}{2} + \theta_r}^{\alpha_{ir} + \frac{\gamma_{tr}}{2} + \theta_r} B_r(\varphi, \theta_r) d\varphi \tag{44}$$

$$\Phi_{or}(i) = R_r^+ .L. \int_{\beta_{ir} - \frac{\gamma_{or}}{2} + \theta_r}^{\beta_{ir} + \frac{\gamma_{or}}{2} + \theta_r} B_r(\varphi, \theta_r) d\varphi \tag{45}$$

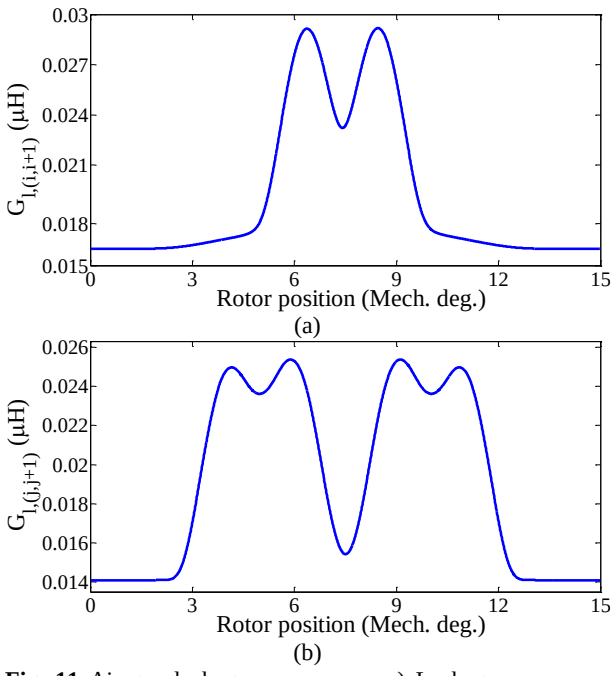

Fig. 11 Air-gap leakage permeances; a) Leakage permeance between two adjacent stator teeth and b) Leakage permeance between two adjacent rotor teeth.

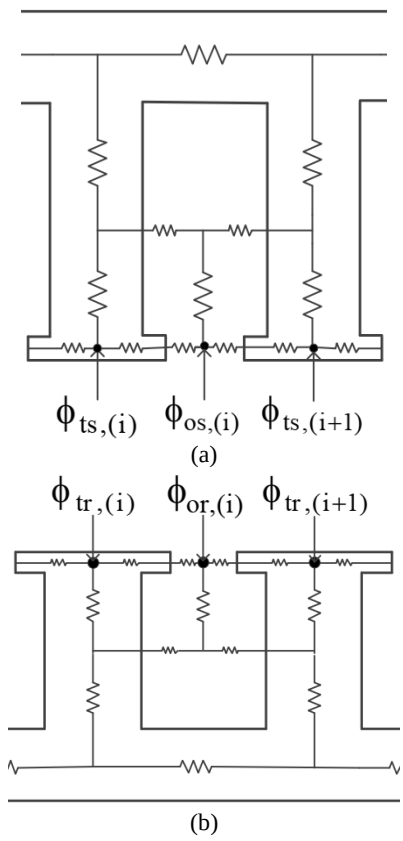

Fig. 12 CMEC models of stator and rotor; a) stator and b) rotor.

where L is the axial length of stator and rotor core, R_s^- is slightly less than the inner radius of the stator, R_s^+ is slightly bigger than the outer radius of the rotor, α_{is} and α_{ir} are respectively the central angle of i-th tooth of stator and rotor, β_{is} and β_{ir} are respectively the central angle i-th slot-opening of stator and rotor, γ_{ts} and γ_{tr} are respectively the angular width of stator and rotor teeth, γ_{os} and γ_{or} are respectively the angular width of stator and rotor slot-openings, B_r is the radial component of the air-gap magnetic field, φ is the circumferential position in stator frame, and θ_r is the rotor position.

The node equations for the CMEC model of stator and rotor can be written as:

$$P_s.F_s = \Phi_s \tag{46}$$

$$P_r.F_r = \Phi_r \tag{47}$$

where P_s and P_r are respectively the permeance matrix of stator and rotor, F_s and F_r are respectively the scalar magnetic potential of stator and rotor, and Φ_s and Φ_r are respectively the input flux matrix into surface nodes of stator and rotor.

After solving the nonlinear equations (46) and (47) using the Newton-Raphson method, the equivalent virtual currents with MMF drops in iron parts of stator and rotor cores are calculated as

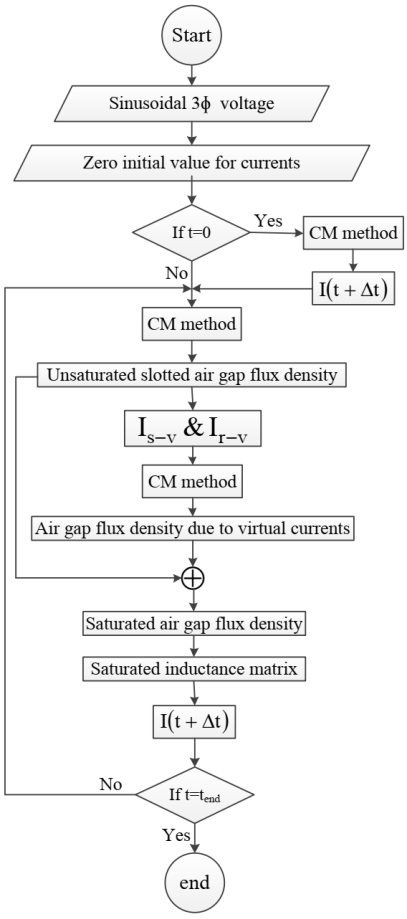

Fig. 13 Simulation flowchart by ICM.

$$I_{s-v}(i) = F_s(i) - F_s(i+1) \tag{48}$$

$$I_{r-v}(i) = F_r(i) - F_r(i+1) \tag{49}$$

where $I_{s-v}(i)$ and $I_{r-v}(i)$ are respectively the virtual currents equal to MMF drop in stator and rotor cores between i^{th} and $(i+1)^{th}$ teeth, which are considered in the center of ith slot-opening of stator and rotor.

Fig. 13 shows the simulation flowchart by using ICM. For a typical rotor position under the steady-state condition, the distribution of virtual stator and rotor currents due to magnetic saturation, and the radial component of air-gap flux density due to them are shown in Fig. 14.

6 Simulation Results and Discussion

In this paper, the stator windings of the proposed WRIM are fed by a three-phase voltage supply of 400 V under rated load while considering the nonlinear cores for the stator and rotor. The simulated stator current and the electromagnetic torque are verified by comparing them with the corresponding experimental results. Fig. 15 shows the experiment setup.

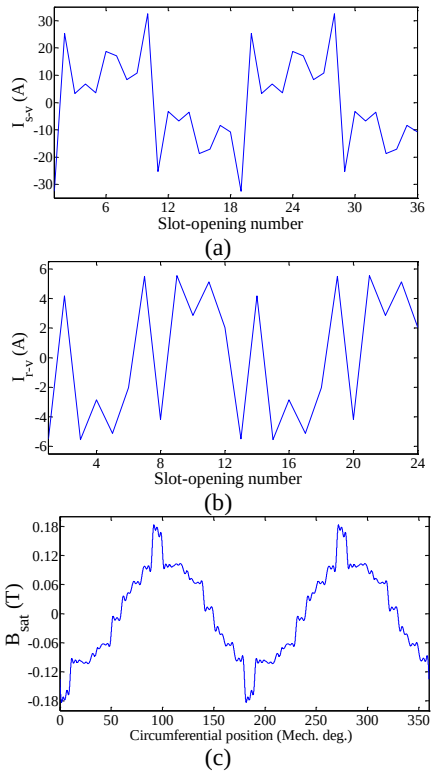

Fig. 14 Equivalent saturation effect used in H-CM.

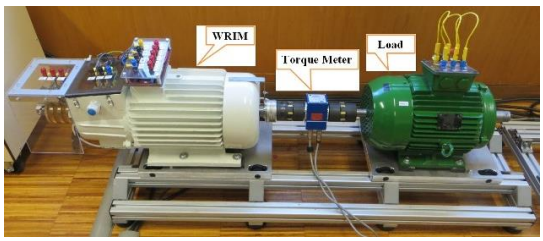

Fig. 15 Experimental Setup.

6.1 Calculation of Inductance

To calculate the inductances of the stator and rotor windings, it is assumed that the rotor is revolving with the rated speed. Then, the self and mutual inductances in terms of the rotor position are calculated using the conventional method as follows:

$$\begin{cases} L_A = \dfrac{\lambda_A}{I_A}\Big|_{I_A \neq 0, I_{B,C,U,V,W} = 0} \\ L_{AB} = \dfrac{\lambda_A}{I_B}\Big|_{I_B \neq 0, I_{A,C,U,V,W} = 0} \end{cases} \tag{50}$$

In (50), λ_A is the flux-linkage of phase A while considering the suitable excitation of the other phases.

Fig. 16 compares the accuracy of the CM, CMEC, IMEC, and FEM for modeling the impact of the rotor slot harmonics on the self-inductance of stator phase 'A' neglecting the magnetic saturation. As shown, the slot harmonics can be accurately modeled using the IMEC and the CM. In fact, the CMEC considers the slot harmonics slightly. Since the rotor has 24 slots, the 12th harmonic is the main time harmonic due to the rotor slotting. Moreover, the DC component of the self-inductance is underestimated using the CMEC about 12%.

Fig. 17(a) compares the saturated self-inductance of the stator phase 'A' obtained through the CMEC, IMEC, ICM, and FEM. The CM method cannot take into account the magnetic saturation; therefore, its result has not been included in Fig. 17. As shown, the DC component of L_{AA} obtained by FEM and IMEC is reduced about 7% due to the magnetic saturation whereas the CMEC and ICM results are reduced about 3% in comparison with Fig. 16(a).

In the ICM method, the magnetic saturation effect is considered with low accuracy compared to CMEC, IMEC, and FEM because the ICM method cannot consider the local magnetic saturation. For this reason, as shown in Fig. 17(a), the result of saturated self-inductance obtained through ICM is higher than the corresponding results of CMEC, IMEC, and FEM. Fig. 17(b) also shows the impact of the magnetic saturation on the other harmonic components of L_{AA}. As shown, the 2nd order harmonic and its multiples are added into the time Fourier spectrum. Fig. 17(b) also shows that the saturation impact is underestimated using the CMEC.

Fig. 18 compares the mutual inductance between the stator phase 'A' and rotor phase 'U' obtained through CMEC, ICM, IMEC, and FEM. As shown, the mutual-inductance is overestimated (about 9%) and underestimated (up to 25%) by the CM and CMEC, respectively. Referring to Fig. 18, the maximum difference between the IMEC result and the FEM result is about 3%.

6.2 Calculation of Phase Current

In the IMEC model, the phase currents of the stator and rotor are obtained by solving the system of equations (1)-(18). However, in the CM method, the phase currents are obtained through solving the system of equations given by (10), (11), (17), (18), (51)-(54).

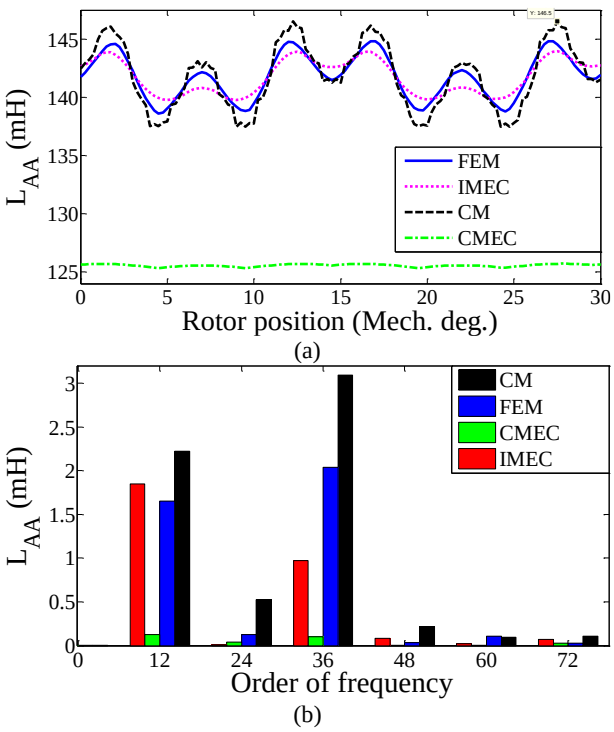

Fig. 16 Unsaturated self-inductance of stator phase A; a) Waveforms and b) Time Fourier spectrum.

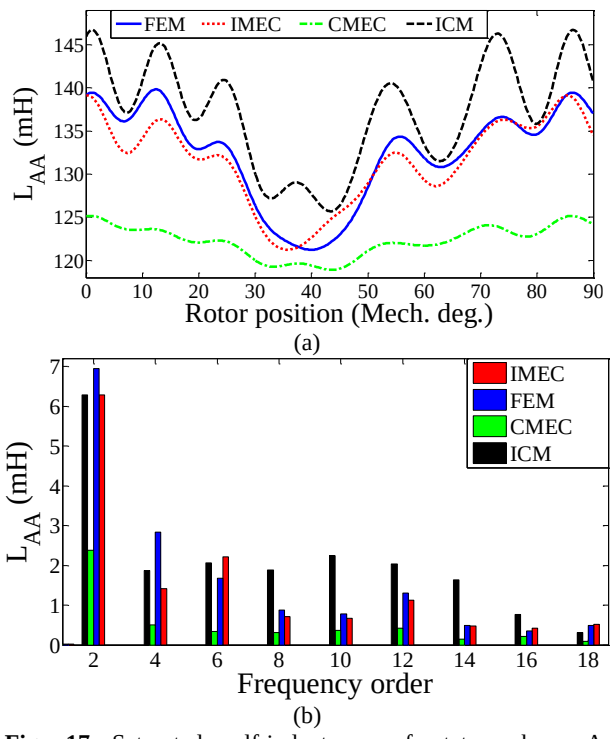

Fig. 17 Saturated self-inductance of stator phase A; a) Waveforms and b) Time Fourier spectrum.

$$\lambda_s = L_{ss} I_s + L_{sr} I_r \tag{51}$$

$$\lambda_r = L_{rs} I_s + L_{rr} I_r \tag{52}$$

$$W_f = \frac{1}{2} L_{ss} I_s^{\,2} + L_{sr} I_s I_r + \frac{1}{2} L_{rr} I_r^{\,2} \tag{53}$$

$$T_e(\theta_r) = \frac{\partial W_f}{\partial \theta_r} \tag{54}$$

where L_{ss}, L_{rr}, L_{sr}, and W_f are respectively the self-inductance matrix of the stator, the self-inductance matrix of the rotor, the mutual inductance matrix, and the stored magnetic energy in the system. Fig. 19 compares the stator phase current (phase 'A') obtained by the ICM, IMEC, FEM, and experiment setup in time and frequency domains under rated load. As shown in Fig. 19, the fundamental component of phase current is underestimated by the ICM about 9.1% whereas the calculated current by IMEC has an error of about 2 percent. In reality, the error seen in Fig. 19 is significantly due to the low accuracy of ICM in modeling the magnetic saturation.

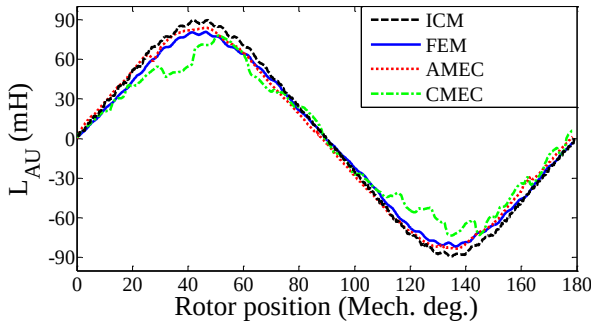

Fig. 18 Saturated mutual-inductance between stator and rotor phases.

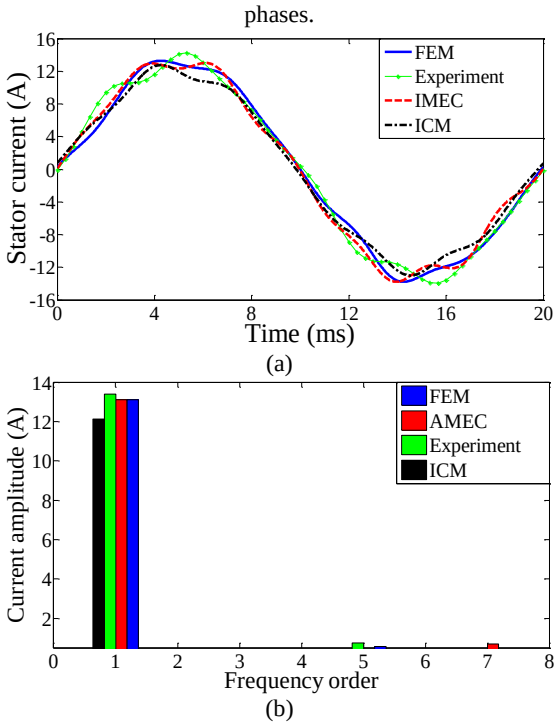

Fig. 19 Stator phase current; a) Waveforms and b) Time Fourier spectrum.

6.3 Calculation of Electromagnetic Torque

The electromagnetic torque (T_e) is calculated using (16) in the CMEC and the IMEC models, and it is calculated using (54) or Maxwell Stress Tensor (MST) method [30] in the CM and ICM method. Fig. 20 compares T_e obtained through ICM, IMEC, FEM, and the experiment under rated load.

As shown in Fig. 15, the torque meter RWT420 is inserted between the rotor shafts of the two motors (WRIM and load), and they are coupled together, then the digital output signal of the torque transducer is transmitted to Laptop through a USB cable. Therefore, the waveform of instantaneous torque is obtained which is equal to the electromagnetic torque of WRIM, in case of neglecting friction torque of WRIM. For clarification, the experimental result is solely shown in Fig. 20(b). Since the 6th harmonic is the dominant harmonic of T_e, it is considered in Table 2 with the DC component for harmonic content comparison. As expected, the torque meter cannot predict the harmonic components of T_e. Table 2 also shows that the IMEC results have good agreement with that of the FEM and experimental results. The DC component is underestimated and the 6th harmonic is overestimated by the ICM due to the low accuracy of ICM for considering the magnetic saturation.

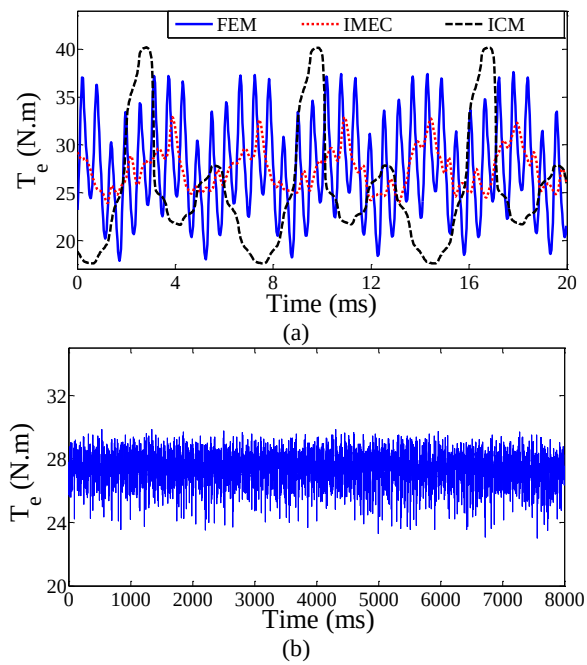

Fig. 20 Electromagnetic torque; a) Waveforms and b) Experiment result.

Table 2 Harmonic content of T_e.

	DC component [Nm]	6th harmonic [Nm]
FEM	27.65	2.146
IMEC	27.81	1.78
ICM	25.17	4.68
Experiment	27.48	Unknown

Table 3 Qualitative comparison.

Model	Slotting effect	Saturation effect	Computation time	User- friendly
CM	Good	Unable	Good	Tolerable
ICM	Good	Average	Good	Tolerable
CMEC	Weak	Good	Very good	Good
IMEC	Good	Good	Very good	Tolerable
FEM	Excellent	Excellent	Weak	Very good
Experiment	Excellent	Excellent	Excellent	Weak

7 Computation Time

The quantitative comparison in terms of the computation time is presented while considering the following conditions for simulation by all techniques.

Time-step = 1/36 ms, Simulation time = 2 s

The general description of hardware (Laptop) is as follows:

Core i5 7400 Intel, 8G RAM

By using CMEC and IMEC, the transient simulation of WRIM takes about 12 minutes while having the air-gap permeances. In CMEC, mutual air-gap permeances are calculated by using Stovic's method, which takes a short time. However, IMEC gets help from the CM method to accurately calculate the mutual and leakage air-gap permeances. Equations (23)-(25) and (34)-(41) are used to this end, which takes less than 1 minute, and it is significant due to SC Toolbox for solving CM_2 (See Fig. 3). The air-gap permeances versus rotor position are calculated once by this technique and stored for future use. Therefore, IMEC and CMEC are both fast techniques.

In the CM and ICM, the relative complex permeance of the slotted air-gap (Λ_s) is once calculated using (23)-(25). The calculation of Λ_s takes less than 1 minute. The field calculation by CM and ICM in each time-step of simulation takes respectively about 0.1 s and 0.12 s because the magnetic field equivalent to saturation effect is also considered in ICM. Therefore, the transient simulation by CM and ICM takes about 2 hr and 2.5 hr, respectively.

The FEM software was used in this paper is Maxwell 16 (64 bit). The FEM discretization consists of 171102 second-order triangular elements. The field and current calculation by the FEM take about 2 s in each step of simulation time. Therefore, the total time of transient simulation by FEM is about 40 hours. The experimental results are also obtained very quickly if the experimental setup was prepared.

8 Conclusion

In this paper, an improved magnetic equivalent circuit (IMEC) model was presented which can be used for modeling all electric machines. In the IMEC model, the iron parts are modeled similar to the CMEC, and the air-gap region is modeled through permeances calculated by CM. Comparison of the obtained results from the CMEC, IMEC, CM/ICM, FEM, and the experiment showed that the IMEC has a good agreement with FEM and experiment results. The results also show that ICM cannot accurately consider the magnetic saturation, although it is an improved model of CM. In Table 3, the above-mentioned techniques are qualitatively compared in terms of the modeling accuracy of slotting and saturation effect, computation time, and being user-friendly.

According to Table 3, the IMEC can accurately consider the slotting effect due to using the CM for modeling the slotted air-gap. The IMEC can precisely take into account the impact of magnetic saturation.

Consequently, the precise modeling of electric machines requires the accurate modeling of the air-gap region and iron parts, simultaneously. For this reason, the saturation effect is underestimated by the CMEC due to its main defect in the air-gap modeling. To accurately consider the slot harmonic, the proposed WRIM was simulated with a short time-step (1/36000 s). However, the analysis was done very quickly by the IMEC.

References

[1] M. V. Terzic, D. S. Mihic, and S. N. Vukosavic, "Impact of rotor material on the optimal geometry of high-speed drag-cup induction motor," *IEEE Transactions on Energy Conversion*, Vol. 31, No. 2, pp. 455–465, Jun. 2016.

[2] M. Ojaghi, M. Sabouri, and J. Faiz, "Analytic model for induction motors under localized bearing faults," *IEEE Transactions on Energy Conversion*, Oct. 2017.

[3] J. Faiz and I. Tabatabaei, "Extension of winding function theory for nonuniform air gap in electric machinery," *IEEE Transactions on Magnetics*, Vol. 38, No. 6, pp. 3654–3657, Nov. 2002.

[4] S. D. Sudhoff, B. T. Kuhn, K. A. Corzine, and B. T. Branecky, "Magnetic equivalent circuit modeling of induction motors," *IEEE Transactions on Energy Conversion*, Vol. 22, No. 2, pp. 259–270, Jun. 2007.

[5] P. Naderi, S. Sharouni, and M. Moradzadeh, "Analysis of partitioned stator flux-switching permanent magnet machine by magnetic equivalent circuit," *International Journal of Electrical Power & Energy Systems*, Vol. 111, pp. 369–381, Oct. 2019.

[6] J. Faiz, S. M. M. Moosavi, M. B. Abadi, and S. M. A. Cruz, "Magnetic equivalent circuit modeling of doubly-fed induction generator with assessment of rotor inter-turn short-circuit fault indices," *IET Renewable Power Generation*, Vol. 10, No. 9, pp. 1431–1440, Oct. 2016.

[7] F. Rezaee Alam and K. Abbaszadeh, "Magnetic field analysis in eccentric surface-mounted permanent-magnet motors using an improved conformal mapping method," *IEEE Transactions Energy Conversion*, Vol. 31, No. 1, pp. 333–344, Mar. 2016.

[8] T. C. O'Connell and P. T. Krein, "A Schwarz–Christoffel-based analytical method for electric machine field analysis," *IEEE Transactions on Energy Conversion*, Vol. 24, No. 3, pp. 565–577, Sep. 2009.

[9] K. J. Binns, P. J. Lawernson, and C. W. Trowbridge, *The analytical and numerical solution of electrical and magnetic fields*. New York: Wiley, 1992.

[10] W. Zhu, B. Fahimi, and S. Pekarek, "A field reconstruction method for optimal excitation of permanent magnet synchronous machines," *IEEE Transactions on Energy Conversion*, Vol. 21, No. 2, pp. 305–313, Jun. 2006.

[11] H. J. Park, H. K. Jung, S. Y. Jung, Y. H. Chae, and D. K. Woo, "Field reconstruction method in axial flux permanent magnet motor with overhang structure," *IEEE Transactions on Magnetics*, Vol. 53, No. 6, pp. 1–4, Jun. 2017.

[12] A. Mollaeian, E. Ghosh, H. Dhulipati, J. Tjong, and N. C. Kar, "3-D sub-domain analytical model to calculate magnetic flux density in induction machines with semi-closed slots under no-load condition," *IEEE Transactions on Magnetics*, Vol. 53, No. 6, pp. 1–5, Jun. 2017.

[13] Z. Q. Zhu, L. J. Wu, and Z. P. Xia, "An accurate subdomain model for magnetic field computation in slotted surface-mounted permanent-magnet machines," *IEEE Transactions on Magnetics*, Vol. 46, No. 4, pp. 1100–1115, Apr. 2010.

[14] Y. Liu, Z. Zhang, W. Geng, and J. Li, "A simplified finite element model of hybrid excitation synchronous machines with radial/axial flux paths via magnetic equivalent circuit," *IEEE Transactions on Magnetics*, Vol. 53, No. 11, Nov. 2017.

[15] A. Hemeida and P. Sergeant, "Analytical modeling of surface PMSM using a combined solution of Maxwell's equations and magnetic equivalent circuit," *IEEE Transactions on Magnetics*, Vol. 50, No. 12, pp. 1–13, Jun. 2014.

[16] D. K. Lim, K. P. Yi, D. K. Woo, H. K. Yeo, J. S. Ro, C. G. Lee, and H. K. Jung, "Analysis and design of a multi-layered and multi-segmented interior permanent magnet motor by using an analytic method," *IEEE Transactions on Magnetics*, Vol. 50, No. 6, pp. 1–8, Jan 2014.

[17] A. Tessarolo, "Modeling and analysis of synchronous reluctance machines with circular flux barriers through conformal mapping," *IEEE Transactions on Magnetics*, Vol. 51, No. 4, pp. 1–11, Apr. 2015.

[18] D. Yan, C. Xia, L. Guo, H. Wang, and T. Shi, "Design and analysis for torque ripple reduction in synchronous reluctance machine," *IEEE Transactions on Magnetics*, Vol. 54, No. 11, pp. 1–5, Jul. 2018.

[19] A. Hanic, D. Zarko, and Z. Hanic, "A novel method for no-load magnetic field analysis of saturated surface permanent-magnet machines using conformal mapping and magnetic equivalent circuits," *IEEE Transactions on Energy Conversion*, Vol. 31, No. 2, pp. 740–749, Jun. 2016.

[20] L. Gu, S. Wang, D. Patil, B. Fahimi, and M. Moallem, "An improved conformal mapping aided field reconstruction method for modeling of interior permanent magnet synchronous machines," *IEEE Energy Conversion Congress and Exposition (ECCE)*, Milwaukee, pp. 1–7, 2016.

[21] Z. Zhang, C. Xia, Y. Yan, Q. Geng, and T. Shi, "A hybrid analytical model for open-circuit field calculation of multi-layer interior permanent magnet machines," *Journal of Magnetism and Magnetic Materials*, Vol. 435, pp. 136–145, Aug. 2017.

[22] D. Zarko, D. Ban, and T. A. Lipo, "Analytical calculation of magnetic field distribution in the slotted air gap of a surface permanent-magnet motor using complex relative air-gap permeance," *IEEE Transactions on Magnetics*, Vol. 42, No. 7, pp. 1828–1837, Jul. 2006.

[23] D. Zarko, D. Ban, and T. A. Lipo, "Analytical solution for cogging torque in surface permanent-magnet motors using conformal mapping," IEEE Transactions on Magnetics, Vol. 44, No. 1, pp. 52–65, Jan. 2008.

[24] T. A. Driscoll and L. N. Trefethen, *Schwarz-Christoffel mapping*. Cambridge University Press, 2002.

[25] V. Ostovic, *Dynamics of saturated electric machines*. Springer-Verlag, 1989.

[26] M. L. Bash, and S. D. Pekarek, "Modeling of salient-pole wound-rotor synchronous machines for population-based design," *IEEE Transactions on Energy Conversion*, Vol. 26, No. 2, pp. 381–392, Jun. 2011.

[27] A. Deihimi, S. Farhangi, and G. Henneberger, "A general nonlinear model of switched reluctance motor with mutual coupling and multiphase excitation," *Electrical Engineering*, Vol. 84, No. 3, pp. 143–158, Jul. 2002.

[28] S. Yavuz, N. Parspour, and L. Ma, "Analytical modeling of a parameterized switched reluctance motor with adapting flux tube method," *International Conference on Industrial Technology (ICIT)*, 2018.

[29] B. N. Cassimere, S. D. Sudhoff, and D. H. Sudhoff, "Analytical design model for surface-mounted permanent-magnet synchronous machines," *IEEE Transactions on Energy Conversion*, Vol. 24, No. 2, pp. 347–357, Jun. 2009.

[30] K. Abbaszadeh and F. Rezaee-Alam, "On-load field component separation in surface-mounted permanent-magnet motors using an improved conformal mapping method," *IEEE Transactions on Magnetics*, Vol. 52, No. 2, pp. 1–12, Feb. 2016.

[31] L. J. Wu, Z. Li, X. Huang, Y. Zhong, Y. Fang, and Z. Q. Zhu, "A hybrid field model for open-circuit field prediction in surface-mounted PM machines considering saturation," *IEEE Transactions on Magnetics*, Vol. 54, No. 6, pp. 1–12, Jun. 2018.

F. Rezaee-Alam received the B.Sc. degree from the Shahid Chamran University of Ahwaz in 2007, the M.Sc. and Ph.D. degrees from the Khajeh Nasir University of Technology in 2010 and 2015, respectively, all in electrical engineering. He is currently an Assistant Professor in the Department of Electrical Engineering, Lorestan University, Iran. His research interests include modeling and design of electric machines.

B. Rezaeealam received the B.Sc. degree from the Isfahan University of Technology in 1997, the M.Sc. and Ph.D. degrees from the University of Tehran in 2000 and 2005, respectively, all in Electrical Engineering. He is currently an Associate Professor in the Department of Electrical Engineering, Lorestan University, Iran. His research interests include modeling and design using FEM, electrical machines, and drives.

S. M. M. Moosavi received the Ph.D. degree from the University of Tehran in 2016 in Electrical Engineering. He is currently an Assistant Professor in the Department of Electrical Engineering, Hamedan University of Technology, Iran. His research interests include modeling, control, and fault diagnosis of electrical machines.

© 2021 by the authors. Licensee IUST, Tehran, Iran. This article is an open access article distributed under the terms and conditions of the Creative Commons Attribution-NonCommercial 4.0 International (CC BY-NC 4.0) license (https://creativecommons.org/licenses/by-nc/4.0/).